JOURNAL OF SYNCHROTRON RADIATION

ISSN 1600-5775

Received 24 May 2016
Accepted 2 September 2016

Edited by G. E. Ice, Oak Ridge National Laboratory, USA

Keywords: beamline; X-ray diffraction; X-ray absorption; total X-ray scattering; resonant X-ray emission.

Supporting information: this article has supporting information at journals.iucr.org/s

XDS: a flexible beamline for X-ray diffraction and spectroscopy at the Brazilian synchrotron

F. A. Lima,[a]* M. E. Saleta,[a] R. J. S. Pagliuca,[a] M. A. Eleotério,[a] R. D. Reis,[a] J. Fonseca Júnior,[a] B. Meyer,[a] E. M. Bittar,[b] N. M. Souza-Neto[a] and E. Granado[c]*

[a]Laboratório Nacional de Luz Síncrotron, Caixa Postal 6192, CEP 13084-971, Campinas (SP), Brazil, [b]Centro Brasileiro de Pesquisas Físicas, Rua Doutor Xavier Sigaud 150, CEP 22290-180, Rio de Janeiro (RJ), Brazil, and [c]Instituto de Física 'Gleb Wataghin', Universidade de Campinas, CEP 13083-859, Campinas (SP), Brazil. *Correspondence e-mail: frederico.lima@lnls.br, egranado@ifi.unicamp.br

The majority of the beamlines at the Brazilian Synchrotron Light Source Laboratory (LNLS) use radiation produced in the storage-ring bending magnets and are therefore currently limited in the flux that can be used in the harder part of the X-ray spectrum (above ∼10 keV). A 4 T superconducting multipolar wiggler (SCW) was recently installed at LNLS in order to improve the photon flux above 10 keV and fulfill the demands set by the materials science community. A new multi-purpose beamline was then installed at the LNLS using the SCW as a photon source. The XDS is a flexible beamline operating in the energy range between 5 and 30 keV, designed to perform experiments using absorption, diffraction and scattering techniques. Most of the work performed at the XDS beamline concentrates on X-ray absorption spectroscopy at energies above 18 keV and high-resolution diffraction experiments. More recently, new setups and photon-hungry experiments such as total X-ray scattering, X-ray diffraction under high pressures, resonant X-ray emission spectroscopy, among others, have started to become routine at XDS. Here, the XDS beamline characteristics, performance and a few new experimental possibilities are described.

1. Introduction

The Brazilian Synchrotron Light Source Laboratory (LNLS) is the first synchrotron light source installed in the southern hemisphere, being in operation since 1997 (Craievich & Rodrigues, 1997; Rodrigues *et al.*, 1998). The LNLS has a storage ring with 93 m circumference operating at 1.36 GeV and 160–250 mA beam current (top-up mode is not available). There are currently 18 beamlines installed at LNLS covering experiments in the soft (lower energy ∼3 eV) and hard X-ray regimes. An endstation dedicated to infrared nanospectroscopy was recently installed, in which both continuous and edge radiations can be extracted from the visible to the THz spectral range (Moreno *et al.*, 2013). The newest beamline at LNLS is dedicated to X-ray tomography and phase contrast imaging (Moreno *et al.*, 2015). Most of these beamlines use radiation from the 1.67 T bending dipoles, with a critical energy of 2.1 keV. Among the techniques available, the most widely used are X-ray diffraction (XRD) to study single crystals, powders and macromolecules; X-ray absorption spectroscopy (XAS); X-ray magnetic circular dichroism (XMCD); and small-angle X-ray scattering (SAXS). Currently, three insertion device (ID) sources (two wigglers and one undulator) are installed at straight sections in the LNLS storage ring, providing X-rays for a macromolecular crystallography beamline (Guimarães *et al.*, 2009), a soft X-ray

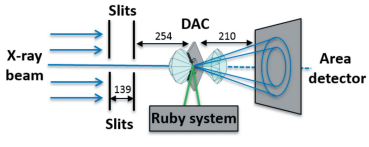

beamline dedicated to the study of surface science (Cezar *et al.*, 2013), and the materials science beamline, the subject of this work.

The superconducting multipolar wiggler (SCW) installed at LNLS was chosen in order to provide users with a significantly higher flux of hard X-rays with respect to the bending-magnet beamlines. This SCW serves as the source for a beamline that meets the needs of the materials science community, in particular with respect to the capability to operate at high energies. This new beamline is named XDS (standing for X-ray Diffraction and Spectroscopy) and is equipped with a versatile optics set and instruments allowing conventional X-ray diffraction and spectroscopy experiments. The XDS beamline operates in the energy range between 5 keV and 30 keV, allowing *K*-edge XAS experiments of most 3*d* and 4*d* metals and *L*-edge XAS of 5*d* metals, actnides and lantanides. The higher photon flux allows XRD experiments also in transmission mode. A wide variety of sample environments is available at the XDS beamline, including cryostats, ovens, pressure cells and external magnetic fields. Additionally, the higher photon flux at XDS compared with the regular LNLS beamlines using bending-magnet sources, in particular at energies around 20 keV and above, makes possible the implementation of photon-hungry experiments, *e.g.* total X-ray scattering experiments that can be analyzed by the atomic pair distribution function (PDF), inelastic X-ray scattering (IXS) and resonant X-ray emission spectroscopy (RXES).

In the following sections we briefly describe the photon source and optical arrangement of the XDS beamline. The experimental hutch and installed equipment, as well as the performance for different configurations, will also be discussed. Some experiments illustrating the capabilities of the beamline regarding challenging and photon-hungry experiments will be presented.

2. Beamline overview

In this section we describe the SCW and the main optical elements installed at the XDS beamline. Owing to the flexible optical scheme, different operation modes can be employed at XDS, resulting in either collimated or focused beams in a wide energy range, which are chosen according to each experiment. A summary of the most commonly used operation modes is presented, together with the beamline performance for each of those modes.

Finally, we describe the experimental station where XAS or XRD can be performed, the XDS beamline capabilities and the equipment installed. Combined XAS–XRD experiments can also be performed, which can be particularly helpful in studies using non-ambient conditions as in the case of *in situ* and *in operando* studies.

2.1. Superconducting wiggler

The photon source for the XDS beamline at LNLS is a superconducting multipolar wiggler manufactured by Budker Institute of Nuclear Physics (Novosibirsk, Russia). The source parameters were optimized using simulations and are described below. The SCW has a total of 35 poles with a period of 60 mm, resulting in a wiggler length of 1.06 m. With a *K* parameter equal to 22.97, a magnetic gap of 18 mm and magnetic field of 4.1 T (4.19 T maximum), the SCW irradiates a total of 5.04 kW of power. Fig. 1 shows the calculated SCW brilliance using the LNLS storage ring parameters compared with the brilliance of the standard 1.67 T bending dipoles. An increase of more than two orders of magnitude is obtained at 10 keV when compared with the brilliance generated at the standard bending dipoles commonly used as photon source at LNLS. This gain in brilliance can go up to four orders of magnitude at 20 keV.

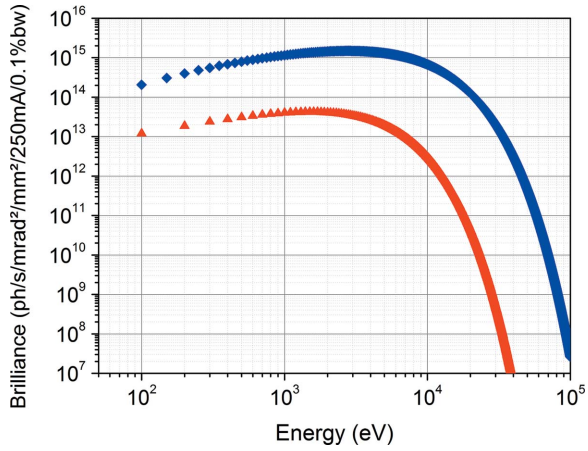

Figure 1
Calculated brilliance generated by the SCW source of the XDS beamline (blue). The brilliance of the standard 1.67 T bending dipoles is also shown (red). Note the increase in brilliance, in particular at energies above 10 keV.

2.2. Beamline optics and operation modes

The XDS is a multi-purpose beamline, with focus on XRD and XAS experiments in the energy range between 5 and 30 keV. Some of the diffraction experiments demand control of the horizontal divergence, which due to the LNLS emmitance is only achievable with sagittal focusing in a double-crystal monochromator. On the other hand, the use of flat crystals and focusing with a toroidal mirror was considered to be the best choice for XAS measurements. These apparently contradictory requirements from the diffraction and absorption community led us to propose a flexible configuration for this beamline. In its basic configuration the beamline operates with a collimating mirror (VCM) with bender, a double-crystal monochromator (DCM) with interchangeable sets of crystals, and a focusing mirror (VFM) with a bending mechanism to allow for focus adjustments. Bruker ASC manufactured all the beamline components present in the optical hutch. An illustration of the optics configuration used at the XDS beamline, as well as the experimental hutch, is given in Fig. 2.

The collimating mirror is located at 11 m from the source. The VCM is a 1.2 m-long silicon mirror operating at a 2.75 mrad incidence angle. It is equipped with a bender

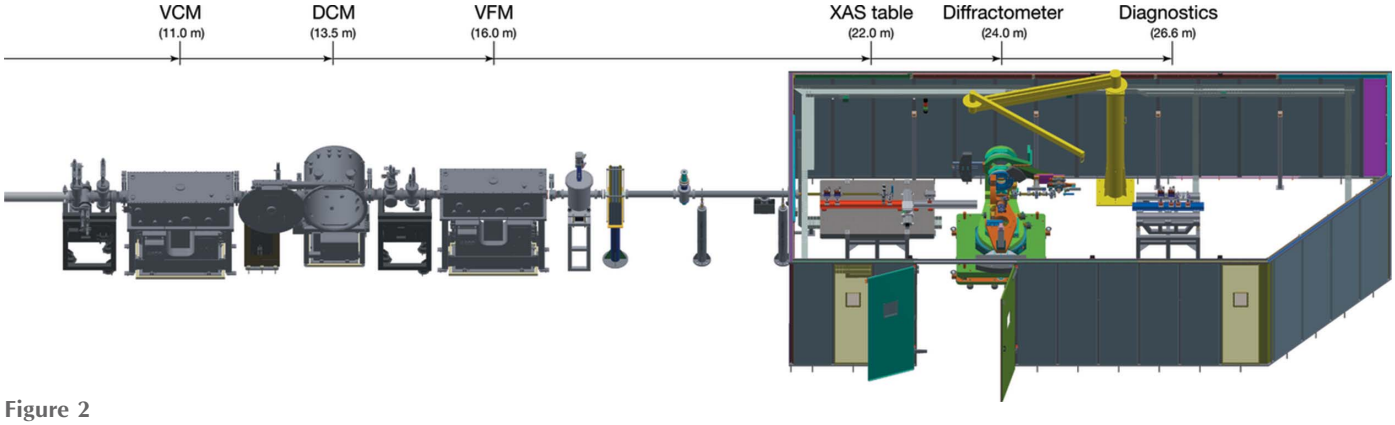

Figure 2
3D layout of the XDS beamline at LNLS showing the optical components and the experimental hutch. Important components are labeled individually: DCM, VCM and VFM. Numbers in parentheses indicate the approximate distance (in meters) of each component from the SCW source.

allowing a cylindrical shape to vertically collimate the beam in order to achieve the highest possible energy resolution, here limited by the Darwin width of the monochromator. In order to cover the whole operating energy range with optimum harmonics rejection, the VCM has three stripes: silicon, rhodium (both with 66 mm width, resulting in 6 mrad horizontal acceptance) and platinum (22 mm width, resulting in 2 mrad horizontal acceptance). In all cases, the bending radius of the VCM is larger than 3.5 km. The heat load in the VCM is dissipated through a water-cooling system.

The monochromator is located downstream of the VCM, at 13.5 m from the source. The DCM is equipped with three crystal pairs: a plane Si(111), a plane Si(311) and a dynamically bent sagittal Si(111). The latter is needed to provide a wide energy range and the collimation control needed by some experiments performed at XDS. The crystals in the first stage of the DCM are cryogenically cooled by LN_2 (indirect cooling by Cu heat exchangers). The DCM is designed to operate between 5 and 20 keV when equipped with either plane or sagittal Si(111) crystals, and between 14 and 30 keV when using the plane Si(311) crystals. The pitch of the second crystal in the DCM can also be fine-tuned by piezo-electric actuators to achieve a better stabilization of the X-ray beam intensity during the experiments.

The focusing mirror is also a 1.2 m-long silicon mirror and is located at 16 m from the source. It operates at 2.75 mrad incidence and is equipped with a dynamical bender to allow focusing of the beam at the sample position. It is coated with three different stripes: a rhodium and a platinum one with 35 mm width and toroidal shape (bending radius larger than 3.5 km and toroidal radius of 29.33 mm) resulting in 2 mrad horizontal acceptance; the third stripe is also coated with rhodium but has a cylindrical shape and 50 mm width, resulting in 6 mrad horizontal acceptance. The different combinations of coatings present in the VCM and VFM allows operation over a wide energy range and, at the same time, minimizes the high harmonic contamination in the beam.

The X-ray beam size at the sample position is about 1.5 mm $\times$ 0.3 mm (horizontal $\times$ vertical) with the toroidal focusing mirror and 2.5 mm $\times$ 0.2 mm (horizontal $\times$ vertical) with the cylindrical focusing mirror. The above configuration allows the XDS beamline to operate in an energy range between 5 and 30 keV with different modes, according to the specific experiment.

2.3. Beamline performance

The optical setups, *i.e.* different configurations of VCM, DCM and VFM in different modes, were designed to maximize the photon flux in the desired energy ranges, accordingly. Photon flux, beam size, beam divergence and energy resolution were calculated using the ray-tracing code *Shadow3* (Sanchez del Rio *et al.*, 2011). The most commonly used operation modes at XDS, that should be chosen by the users according to the specific experiment, are detailed in Table 1. Modes A and E use the sagittally bent Si(111) monochromator, and are more appropriate for diffraction experiments. The only difference between modes A and E is the VCM used, operating with Si or Rh stripes, respectively. This is used to prevent higher harmonics contamination during the experiment, as the VCM operating with 2.75 mrad incidence angle results in an energy cutoff of about 11.5 keV and 23 keV in the case of the Si or Rh stripes, respectively. Modes B, C and D use plane crystals in the monochromator, with B and C operating with a Si(111) and D with a Si(311) crystal pair. These modes exploit the toroidal focusing and are mostly used in spectroscopy experiments. Again, the difference between modes B and C is only the VCM used, Si for mode B and Rh for mode C; the appropriate choice is made to minimize the higher harmonics content in the beam. Mode D uses a Si(311) plane monochromator and both VCM and VFM operating in the Pt stripe, being more appropriate to operation above 14 keV due to the Pt absorption edges.

The measured photon flux of the XDS beamline in five different optical configurations (operation modes) is shown in Fig. 3. They were measured using a calibrated AXUV photodiode (Hamamatsu, model S3584-09) and agree within less than a factor of two with the calculations. The maximum flux at XDS is $\sim 10^{13}$ photons s^{-1} $(100\ mA)^{-1}$ and is reached at about 12 keV.

Below we present the experimental hutch configuration, and the results of two conventional XAS and XRD experi-

Table 1
Beamline operating modes.

Mode	Energy range (keV)	Collimating mirror Stripe coating / angle (mrad) Shape	Double-crystal monochromator First crystal cut Shape	 Second crystal cut Shape	Focusing mirror Stripe coating / angle (mrad) Shape
A	7–10	Si / 2.75 Cylindrical	Si(111) Plane	Si(111) Sagittally bent	Rh / 2.75 Cylindrical
B	5–10	Si / 2.75 Cylindrical	Si(111) Plane	Si(111) Plane	Rh / 2.75 Toroidal
C	10–20	Rh / 2.75 Cylindrical	Si(111) Plane	Si(111) Plane	Rh / 2.75 Toroidal
D	14–30	Pt / 2.75 Cylindrical	Si(311) Plane	Si(311) Plane	Pt / 2.75 Cylindrical
E	9–20	Rh / 2.75 Cylindrical	Si(111) Plane	Si(111) Sagittally bent	Rh / 2.75 Cylindrical

ments using standard samples in order to benchmark the beamline performance in real experiments are presented in the supporting information.

2.4. Experimental hutch and regular setups

The XDS experimental hutch has an area of about 37 m^2 and accommodates all the instrumentation to perform XAS and XRD experiments under different experimental conditions (temperature, pressure, magnetic field, atmosphere). A 1.8 m × 1.2 m optical table accommodates the regular XAS experiments, whereas a heavy-duty diffractometer is used for the XRD experiments. The diffractometer is located at the optimum focal position when operating with modes A or E [Si(111) sagittal monochromator and cylindrical VFM at 2.75 mrad incidence angle], at 24 m from the source; however, the focal spot can also be adjusted at other positions by altering the VFM incidence angle and using its bending mechanism. Downstream from the diffractometer the experimental hutch has extra room reserved for unconventional experiments and future upgrades.

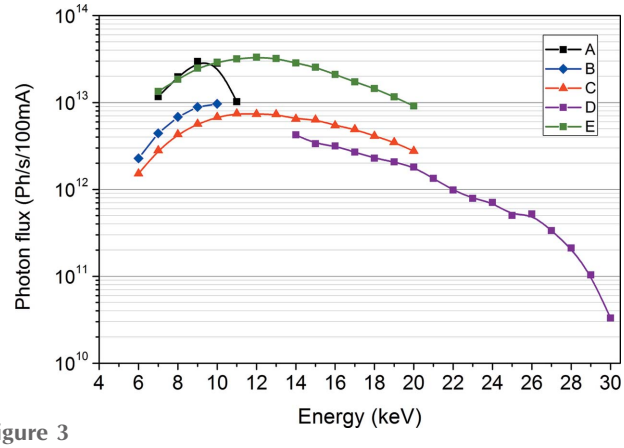

Figure 3
Measured photon flux as a function of energy. The different modes represent the diverse optical setup denoted as VCM–DCM–VFM. The details of each mode are given in Table 1. Note that in some modes (*e.g.* C) the energy range shown is larger than that recommended and might contain higher harmonic contamination.

At 22.0 m from the source the optical table (hereafter called XAS table) houses the equipment necessary for conventional XAS experiments, *i.e.* the detectors (ion chambers, photodiodes, fluorescence detectors, *etc.*) and different sample environments (cryostats, ovens, magnets, *etc.*). The XAS table is equipped with a vertical/horizontal sample stage that can hold up to 45 kg. This stage has a long horizontal travel distance of 500 mm that allows fast setup changes by taking equipment out of the beam path in case XRD experiments are to be performed in sequence. On top of this, another small XY stage capable of holding up to 2 kg can be mounted if shorter/faster movements are needed.

A 12-element SiLi fluorescence detector (Princeton Gama Detector) is available for XAS in fluorescence mode. A home-made oven and gas system (with controllers, gas detectors, exhaust, *etc.*) can be used to perform *in situ* or *in operando* catalysis studies or other XAS experiments in transmission mode varying the temperature (up to 1200 K) and atmosphere. Alternatively, different types of flow microreactor using capillaries can also be used (Figueroa *et al.*, 2013; Rodella, 2015).

Located at 24.0 m from the SCW there is a low-magnetic 6+2-circle Huber diffractometer (modified model 5021). The diffractometer is installed on a lifting and laterally translating table. This table allows for the correct positioning of the X-ray beam in the center of the diffractometer. For regular XRD and total X-ray scattering experiments either flat plates or capillary tube samples can be mounted on a goniometer head, working in Bragg–Brentano or Debye–Scherrer geometries, respectively. Those experiments can be performed either in high-resolution or high-intensity modes. In the high-resolution mode different crystal analyzers can be chosen in combination with a LaBr scintillator (FMB Oxford) according to the experimental needs. The XDS high-resolution diffraction analyzers available include Si(100), Si(110), Si(111), Ge(100), Ge(110), Ge(111), Al(100), Al(110), Al(111), Cu(110) and Cu(111) crystals. Highly ordered pyrolytic graphite (HOPG) analyzers are also available, suitable for experiments in the high-intensity mode. In addition, the 2θ arm of the Huber

diffractometer can house an X-ray polarization analyzer (Huber GmbH). This polarimeter, when used in combination with the appropriate analyzer(s), allows measurements of the diffracted beams with σ and π polarization. Alternatively, the XRD and total scattering experiments can employ linear strip detectors. A Dectris Mythen 6K system composed of six individual Mythen 1K detectors housed in an aluminium case is available for users (Schmitt *et al.*, 2003, 2004; Bergamaschi *et al.*, 2010). The Mythen 6K system covers a range of $2\theta \simeq 28^\circ$ in a single measurement, which allows collecting good quality diffraction patterns in very short periods of time (about 5–10 s). This is useful for *in situ* and *in operando* experiments or to follow the kinetics of crystallization during deposition/growing of thin films in real time. If necessary, a regular individual Mythen 1K can also be used. The XDS is also equipped with two different two-dimensional detectors: a Pilatus 300K (Dectris Ltd) and a MarCCD MX225 (Rayonix, LLC). Finally, the Huber diffractometer is capable of holding different accessories that permit mounting of non-ambient sample environments.

For investigations involving special thermal environments, the XDS beamline has two commercial pieces of equipment: a closed-cycle He Joule–Thomson Cryostat (AS Scientific) and a HTK 1200N Oven-Chamber with Capillary Extension (Anton Paar). The temperature range of the cryostat is between <2 K and 300 K and the oven operates from room temperature up to 1473 K. The beamline is also equipped with a 6 T superconducting cryogen-free magnet (HTS-11) for XRD experiments with external magnetic field. Moreover, the XDS beamline also disposes of different equipment to perform XRD experiments in Debye–Scherrer configuration with temperature control: a hot air blower (FMB Oxford) that can operate from 298 to 1273 K and a CryoJet (Oxford) with an operation range between 80 and 500 K. The former can also be combined with a capillary cell for controlling the atmosphere

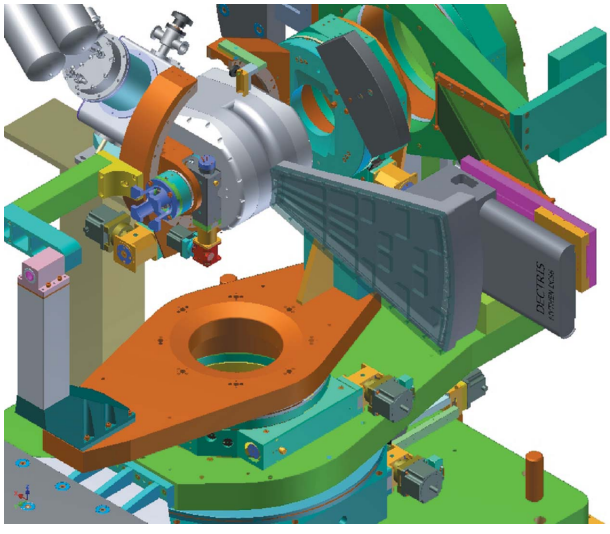

Figure 4
Illustration of the Huber diffractometer of the XDS beamline at LNLS equipped with the 6 T superconducting magnet and the Mythen 6K system.

(Rodella, 2015). All this equipment is compatible with the Huber diffractometer, whereas the closed-cycle cryostat and the air blowers can easily be placed in the XAS table using existing adapters and/or the sample stages. In the case of experiments at non-ambient pressures, the beamline offers a complete setup for high-pressure experiments up to 80 GPa (currently limited by the minimum beam size obtained by using a slit system; see §3.2), including membrane and screw diamond anvil cells (DAC), an online pressure-calibration system using ruby fluorescence and a cryostat compatible with the DACs. An illustration of the Huber diffractometer set with the Mythen 6K and the 6 T superconducting cryogen-free magnet (supported directly in the Huber base) is shown in Fig. 4.

The whole beamline, including the optics, monochromator, diffractometer and experimental data collection, is operated using *SPEC* software (Certified Scientific Software) in a Linux environment PC.

3. New experimental possibilities at LNLS using XDS beamline

In this section we present some experiments performed at the XDS beamline to illustrate the capabilities of the beamline.

3.1. X-ray total scattering

Analysis of X-ray total scattering data by pair distribution function (PDF) has been used to study amorphous phases of materials, *i.e.* those with XRD patterns presenting broad and low-intensity Bragg peaks. Good examples of materials that can be investigated by PDF are nanomaterials in general. PDF is a powerful technique that provides information on the local and medium-range order of the materials under study. More information about PDF can be found in the book by Egami & Billinge (2003).

To obtain good total scattering data to be analyzed by the PDF technique some directions should be followed: (i) reaching high momentum transfer (Q), preferably higher than 20 Å^{-1} (ideally 40 Å^{-1} or more); however, many successful experiments with synchrotron radiation and in-house equipment employing Mo and Ag anodes reaching only a Q-value of 20 Å^{-1} have been reported (Haverkamp & Wallwork, 2009; Ingham, 2015; Petkov *et al.*, 2013; Dykhne *et al.*, 2011); (ii) obtaining high resolution in Q and good statistics (high signal-to-noise ratio) for high Q-values; and, finally, (iii) using instruments with low background noise, since the data need to have a better signal-to-noise ratio than for Rietveld refinement (Billinge, 2004; Petkov, 2012). All of these experimental recommendations can be easily obtained at the XDS beamline.

An X-ray total scattering experiment was performed using silver nanoparticles (Ag NPs). The nanoparticles were produced by chemical reduction of silver nitrate using trisodium citrate as reduction agent (Lee & Meisel, 1982; Rivas *et al.*, 2001). The UV–Vis spectra of the obtained Ag sol presented an absorption peak at ~400 nm, typical of the

plasmon resonance of Ag NPs with diameters around 15 nm (Bastús *et al.*, 2014; Agnihotri *et al.*, 2014; Henglein, 1979). By dynamic light scattering (DLS), a hydrodynamic diameter of ∼11 nm was determined. In addition to the population of 11 nm, another population of around 70 nm which might constitute agglomerates of the primary particles was also noticeable by DLS. The X-ray total scattering data was collected in Debye–Scherrer configuration at room temperature. The X-ray energy was set to 20 keV. Detection of the diffracted photons was carried out by using a HOPG analyzer in combination with a standard LaBr scintillator in a 2θ interval of 1° up to 160°, corresponding to a maximum $Q \simeq 20$ Å^{-1}. This setup allows a good resolution in Q-space to be obtained compared with other setups which use large area detectors and higher X-ray photon energies (above 60 keV). Additionally, the good Q-space resolution obtained by our setup results in the avoidance of mathematical dampening which can make data analysis difficult and allows the study of very high interatomic distances reaching the mesoscale region (Petkov, 2012). Although the XDS beamline reaches energies as high as 30 keV (in mode D), the photon flux at this energy is at least two orders of magnitude lower than at 20 keV using sagittal focusing as in mode E (see Fig. 3). Thus, it is preferable to measure at 20 keV and obtain a better signal-to-noise ratio and compromise the maximum Q-value. The Ag powder was mounted inside a boron glass capillary tube (0.3 mm inner diameter and 0.01 mm wall thickness), which was continuously spun to minimize grain size statistical problems. In addition to the Ag sample data, an empty capillary was also measured under the same experimental conditions in order to discount any signal not originating from the Ag sample (capillary, air scattering, *etc.*). This is a standard procedure used in PDF analysis.

The total scattering function, $S(Q)$, computed using the software *PDFgetX3* (Juhás *et al.*, 2013) is presented in Fig. 5. The signal-to-noise ratio in this data is sufficient to provide useful data for PDF analysis up to the highest Q-value of ∼20 Å^{-1}. Also shown in the same figure (inset) is the reduced structure function, $F(Q) = Q[S(Q) - 1]$. This is a useful quantity in PDF analysis, aiding in diagnosing problems with the data or its processing protocol. For example, a bad data set for PDF analysis would include an excessive noise level at high Q-values and/or oscillations in the baseline.

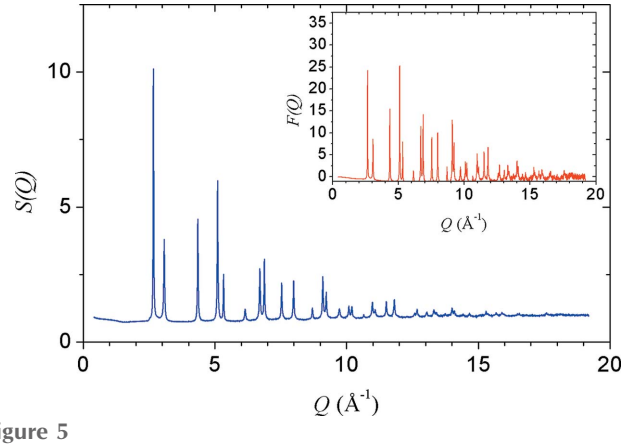

Figure 5
Total scattering function, $S(Q)$, and reduced structure function $F(Q)$ (inset) for silver nanoparticles recorded at room temperature.

The atomic PDF, or the reduced PDF, $G(r)$, will be used throughout this work. It is defined as the Fourier transform of the total scattering intensity as follows (Egami & Billinge, 2003),

$$G(r) = \frac{2}{\pi} \int_{Q_{\min}}^{Q_{\max}} Q[S(Q) - 1] \sin(Qr)\, \mathrm{d}Q. \quad (1)$$

The acquired and normalized patterns were converted into the reduced PDF [$G(r)$] with the software *PDFgetX3*. To fit the experimental $G(r)$ obtained after the processing with *PDFgetX3*, we employed the *PDFfit2–PDFgui* package (Farrow *et al.*, 2007). We fitted all the structural parameters, respecting the symmetry of the compound. We also adjusted the scale factor, the Gaussian dampening factor (Q_{damp}) and the peak broadening. In the peak broadening ($\sigma_{i,j}$) only the coefficient δ_1 for the $(1/r)$ contribution to the peak sharpening was fitted (Farrow *et al.*, 2007).

In Fig. 6 the PDF curve of the Ag NPs is presented, showing the different Ag–Ag distances in the structure. The peaks

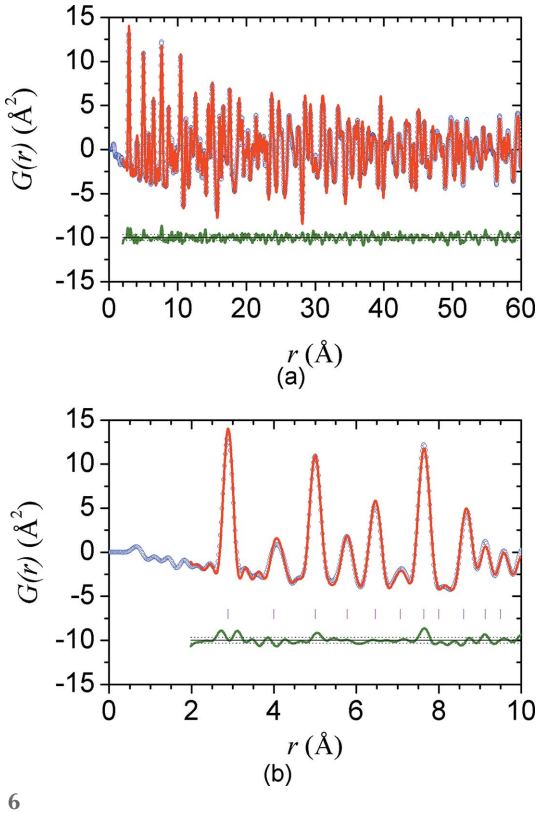

Figure 6
PDFs of silver nanoparticles of diameter ∼11 nm. (*a*) Complete fitted region and (*b*) low r-value. Experimental (circle) and refined (continuous red line) PDF are shown. Below the curve are presented the difference (continuous green line), the mean value (solid black line) and the standard deviation (dashed line) of the difference. $G(r)$ is shown scaled by the factor refined in PDF analysis. In (*b*) the vertical lines show the different peaks associated with the Ag–Ag distances; the additional oscillations correspond to mathematical artifacts from the Fourier transform.

(ripples) which occur at r below ~2.0 Å have no physical meaning. Generally, these peaks are spurious termination ripples resulting from the Fourier transform truncation. This Fourier transform truncation effect becomes less pronounced with increasing r-value and these spurious ripples tend to reduce their intensity, thus they do not significantly affect the PDF analysis. It is important to notice that this is a general effect, occurring in all experimental data analyzed by PDF.

The experimental $G(r)$ data were fitted using the cubic $Fm\bar{3}m$ structure for the metallic silver previously reported (Swanson & Tatge, 1953). The cell parameter obtained from the fitting of the PDF curve is a = 4.0869 (6) Å; this value is somewhat higher than that reported in the literature (4.0862 Å; Swanson & Tatge, 1953), but this behavior is expected in nanostructured materials. Our PDF analysis allowed the extraction of the isotropic thermal displacement, U_{iso}, which converged to a value of 0.0133 (7) Å^2. The fit of the PDF curve converged with R_w = 11.5% and a reduced χ^2 = 0.0078. This demonstrates that the PDF analysis of total X-ray scattering data measured at XDS is of good quality to ensure a proper structural analysis of nanostructured materials. In principle, this experiment could be performed at any bending-magnet beamline at LNLS; however, due to the critical energy of only 2.1 keV the X-ray flux at high energies is severely compromised, hindering the possibility to achieve at least Q = 20 Å^{-1}. Moreover, our setup allows anomalous PDF studies to be performed, *i.e.* X-ray total scattering experiments with energies close to the absorption edge of an element in the sample. A similar experiment has been performed previously at LNLS using lower energies in a regular dipole beamline (de Lima *et al.*, 2013, 2016), however with a lower value of maximum Q-value.

3.2. X-ray diffraction at high pressures

The scientific community has witnessed an unprecedented surge in high-pressure research that greatly improved the fundamental understanding of materials under high compression. Research has benefited from the integration of high-pressure, high- and low-temperature instrumentation and analytical probes at synchrotron facilities. While at other third-generation synchrotrons state-of-the-art high-pressure experiments have been implemented during the last two decades, this is an area to grow at LNLS. With that in mind we have made available at the XDS beamline a setup for XRD experiments under pressures of up to 80 GPa, so far limited by the minimum beam size possible.

In order to apply high pressures at the sample we use a diamond anvil cell (DAC) with the sample between the small tips of the diamonds where a metallic gasket holds the sample while the X-rays transmit through the diamonds and sample. The smaller the tip of the diamonds the higher the pressure one can apply to the sample with the same force to the DAC. At the XDS beamline the focusing optics and superconducting wiggler source produce a focused beam size incompatible with DAC experiments. To overcome this we have used two sets of slits, as shown in Fig. 7, to collimate and define a beam size of about 100 µm × 100 µm at the sample position. This beam size allows using diamond anvils as small as 350 µm diameter, with which pressures of up to 80 GPa have been achieved.

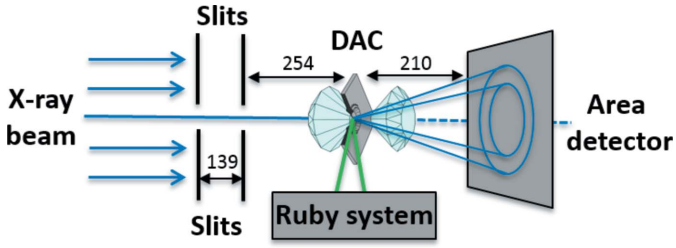

Figure 7
Schematic drawing of the setup for XRD experiments under high pressure at the XDS beamline. The X-rays beam size (100 µm × 100 µm) is defined by two sets of slits. An area detector collects the diffraction pattern from the sample. An optical system placed on the side is used to calibrate the pressure using the ruby luminescence method by rotating the DAC by 90° relative to the original angle used to collect the X-ray diffraction data. Dimensions are given in millimeters.

This method of slitting the beam results in a loss of about two orders of magnitude in photon flux; however, complete powder XRD patterns with good quality can be obtained in a single acquisition by using a CCD detector (RAYONYX SXS165) placed downstream of the DAC. The two-dimensional images are then integrated to provide intensity as a function of 2θ using the software *FIT2D* (Hammersley *et al.*, 1996). Due to the current tungsten carbide seats used in the DAC, which are opaque to X-rays, there is a limited scattering angle range of 25° in 2θ. Therefore the ideal beam energy should be the highest possible in order to probe as many Bragg peaks as possible at these low opening angles. With the compromise of keeping the photon flux as high as possible, the energy is usually set to 19–20 keV using the sagittal Si(111) monochromator. Initially, a mixture of 4:1 methanol–ethanol was used as pressure-transmitting medium to provide quasi-hydrostatic conditions of up to 10 GPa, but currently a gas loading system is available to use Ne or He gases as pressure-transmitting media for hydrostatic conditions at very high pressures. Experiments at low temperatures are possible placing a membrane-driven DAC in contact with the cold finger of a cryostat, which allows the pressure to be applied in the DAC at low temperatures and *in situ* calibrating pressure by the ruby luminescence method (Syassen, 2008).

To benchmark the XRD experiments at high pressures we used the compound $EuGa_4$. We recently reported an isostructural ytterbium-doped compound, $Eu_{0.5}Yb_{0.5}Ga_4$, with electronic and magnetic properties that are dramatically affected by external pressure (Loula *et al.*, 2012). We showed that the insertion of Yb on the $EuGa_4$ compound only induced a contraction of the lattice but without chemical alterations; therefore the changes on the electronic and magnetic properties are only related to europium ions and should also be present on the 'pure' $EuGa_4$ compound. Our XANES results showed that the valence of Eu ions continuously changes from 2+ towards 3+ as pressure is increased. For pressures up to 12 GPa, we clearly observed that the magnetic ordering of the europium magnetic sublattice is changed from anti-

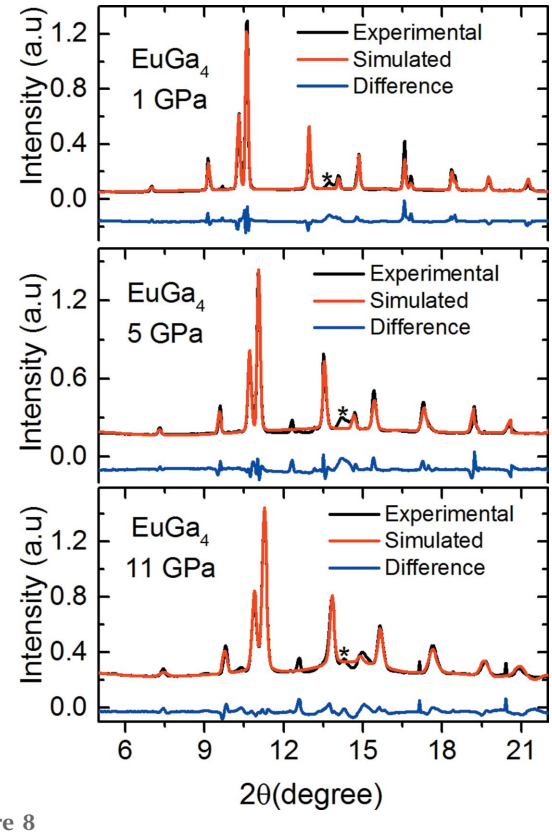

Figure 8
Experimental and simulated XRD patterns of a powdered $EuGa_4$ sample at 300 K for some selected pressures. The broad extra peak near 14° (indicated by * in the figure) is due to the small amount of Ga excess present on the surface of the crystals in the as-grown samples. All the other extra peaks come from the stainless-steel gasket.

ferromagnetic (AFM) to ferromagnetic (FM). However, the behavior of the crystalline structure under pressure is still missing which justified the high-pressure diffraction experiments, now possible at the XDS beamline.

Fig. 8 shows experimental XRD patterns for the $EuGa_4$ sample under some selected pressures (1, 5 and 11 GPa). Also shown in this figure are the corresponding calculated XRD patterns using the Rietveld method. Often, the small amount of sample involved in experiments under pressure with microfocused beam induces a poor powder average in the data, resulting in disagreement of the diffraction peaks intensity relationship. This makes the application of Rietveld analysis limited in such cases. However, here the good agreement between the experimental and calculated XRD patterns shows the quality of our data. Our results show that the $BaAl_4$ structure of $EuGa_4$ is not altered by pressures up to 11 GPa, whereas the crystal lattice is gradually compressed.

While we argue that no structural transition is present in this pressure range based on the Rietveld analisys, the dependence of unit cell volume with pressure does show an anomalous drop around 4 GPa, as shown in Fig. 9, together with the pressure dependence of the *c*/*a* ratio. As mentioned before, our previous results for the parent compound $Eu_{0.5}Yb_{0.5}Ga_4$ show that the magnetic ordering of the europium ions is changed from AFM at ambient pressure to FM at

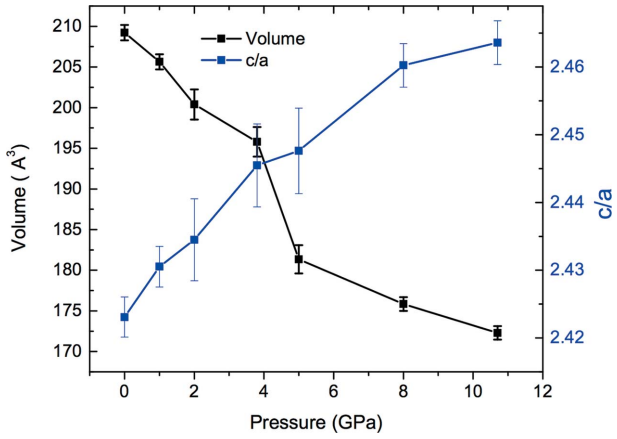

Figure 9
Evolution under pressure of the unit cell volume and the *c*/*a* ratio obtained by Rietveld refinements.

12 GPa. Our XRD results demonstrated that indeed this transition occurs at lower pressures and we argue that this anomalous drop in the volume is likely related to electronic instabilities of the compound that are not strong enough to induce a structural phase transition. This was also observed in other similar systems (Souza-Neto *et al.*, 2012), for which when even higher pressures were applied then it was sufficient to induce the structure to change.

Furthermore, the increase in the *c*/*a* ratio (blue curve in Fig. 8) indicates that the *a*-axis is being more contracted than the *c*-axis. Under ambient pressure, the compound is formed by alternate planes of europium which align antiferromagnetic in the plane. The abrupt change of the unit cell volume switches the sign of the RKKY (Ruderman–Kittel–Kasuya–Yosida) coupling and consequently the type of magnetic ordering. These results conclusively show that the electronic and magnetic transitions previously reported are directly related to the structural modifications presented in this study.

3.3. Resonant X-ray emission spectroscopy

X-ray emission spectroscopy (XES) with improved energy resolution analyzes the details of the emitted photons after the excitation of a core level. XES techniques in the hard X-ray regime are becoming very common at synchrotron and free-electron laser (XFEL) sources, now being used to perform regular non-resonant X-ray emission spectroscopy, resonant inelastic X-ray scattering (RIXS), resonant X-ray emission (RXES), high-energy-resolution fluorescence-detection XAS spectroscopy (HERFD-XAS) and valence-to-core spectroscopy (VtC) experiments (Kotani & Shin, 2001; Eisenberger *et al.*, 1976; Hämäläinen *et al.*, 1991; Bergmann *et al.*, 2001; Safonova *et al.*, 2006; Nemoshkalenko *et al.*, 1968; Döring *et al.*, 2004; Safonov *et al.*, 2006).

High-energy-resolution XAS/XES experiments require a total experimental resolution lower than the natural lifetime of the excited-state or the emitted fluorescence line, respectively. This core-hole lifetime scales almost exponentially in the case of a 1*s* core-hole of transition metals (Krause &

Oliver, 1979; Hämäläinen *et al.*, 1991), resulting in a significant spectral broadening of the near-edge XAS and the consequent emission lines. An interesting way to reduce the apparent broadening caused by core-hole lifetime effects was initially proposed by Hamalainen in 1991 (Hämäläinen *et al.*, 1991) and later theoretically demonstrated by Tanaka *et al.* (1994). The use of a high-resolution spectrometer equipped with curved crystal analyzers allowed the separation of the different emission lines, resulting in XAS spectra with broadening dominated by the intermediate-state lifetime, rather than that of the initial state. This way, an enhanced sensitivity on the measured XAS/RXES/RIXS spectral shape can be obtained (Meisel *et al.*, 1989; Glatzel & Bergmann, 2005; Rueff & Shukla, 2013; Ament *et al.*, 2011). The use of similar high-resolution spectrometers in X-ray emission experiments was pioneered by Bergmann and co-workers (Bergmann *et al.*, 1999, 2001; Glatzel & Bergmann, 2005). A more detailed derivation and examples of lifetime effects in X-ray spectroscopy experiments is given by de Groot (2001), de Groot & Kotani (2008) and Glatzel *et al.* (2013), and a review of the current status and future perspectives of high-resolution spectrometers is given by Kowalska *et al.* (2016*b*).

At the XDS beamline a RXES spectrometer was installed, operating in von Hamos geometry, *i.e.* dispersing the emitted energy using a cyllindrically bent crystal analyzer and detecting the scattered/fluorescence photons using an area detector. This spectrometer design is very similar to others reported elsewhere, including those installed at XFELs (Hoszowska & Dousse, 2004; Szlachetko *et al.*, 2012; Alonso-Mori *et al.*, 2012, 2015; Mattern *et al.*, 2012; Kern *et al.*, 2014). The analyzer dimensions are 10 cm × 5 cm (horizontal × vertical), with bending radius of 25 cm and the emitted X-rays were recorded by a Pilatus 300K detector. Since the setup is flexible, the analyzer dimensions and bending radius could be varied according to the experimental needs. Alternatively, a regular Johansson-type spectrometer can be set using the Huber diffractometer. Currently, this arrangement allows only one spherical analyzer crystal, with radius of curvature ranging from about 0.4 m up to 1.0 m.

In order to demonstrate the capabilities of the RXES spectrometer at the XDS beamline, we used it to record $L\alpha$ RXES data of hexachloroplatinic acid $\{[H_3O]_2[PtCl_6](H_2O)_x\}$ around the platinum L_3 absorption edge. This was done by positioning a Si(100) crystal at a Bragg angle of about 76.2° and recording the (800) diffraction, corresponding to an energy of approximately 9.40 keV. The vertical size of the analyzer crystal and the detector dictate the energy range covered by the RXES spectrometer. In this configuration this range was from 9.23 keV up to 9.66 keV, which was enough to detect both the Pt $L\alpha_1$ and $L\alpha_2$ emission lines. By scanning the monochromator energy around the Pt L_3-edge a complete RXES map was measured, as shown in Fig. 10.

The details of the electronic information content and how it can be obtained by analyzing RXES planes is the subject of numerous works and will not be covered here. For further details the reader is referred to the literature (Glatzel *et al.*, 2004, 2013; Hall *et al.*, 2014). In the RXES data shown in Fig. 10 the presence of two strong resonances at emitted energies of about 9.44 keV and 9.36 keV is clear, for an incoming energy of about 11.56 keV. These correspond to the core transition $2p_{3/2} \rightarrow 5d$ in the Pt atom which generates the L_3 absorption edge, and the consequent emissions $L\alpha_1$ ($3d_{5/2} \rightarrow 2p_{3/2}$ transition) and $L\alpha_2$ ($3d_{3/2} \rightarrow 2p_{3/2}$ transition). It is worth mentioning that the $L\alpha_2$ emission line has an intensity about ten times smaller than that of the $L\alpha_1$, thus long integration times (60 s per incoming energy) were used in the data acquisition in order to improve the statistics in the $L\alpha_2$-detected XAS data. In Fig. 10 two XAS spectra are shown which were extracted from the RXES plane: one total fluorescence yield (TFY) spectrum that was constructed by integrating the full X-ray emission intensity at each beam energy and one high-energy-resolution XAS (HR-XAS) that was obtained by selecting only the signal of the maximum of the $L\alpha_1$ emission line to construct the XAS. The effect of sharpening of the near-edge features in this type of experiment was predicted in 1991 by Hämäläinen and co-workers (Hämäläinen *et al.*, 1991). As expected, the HR-XAS exhibits sharper and more pronounced features, allowing the extraction of detailed electronic structure.

Alternatively, the RXES spectrum can be presented using a constant energy transfer axis ($E_{\rm incoming} - E_{\rm emission}$). In this mode, the cuts along the energy transfer result in spectra with final states equivalent to those of the M_4- and M_5-edges. Additionally, the effects of core-hole spectral broadening can be easily separated from those arising from the instrumental

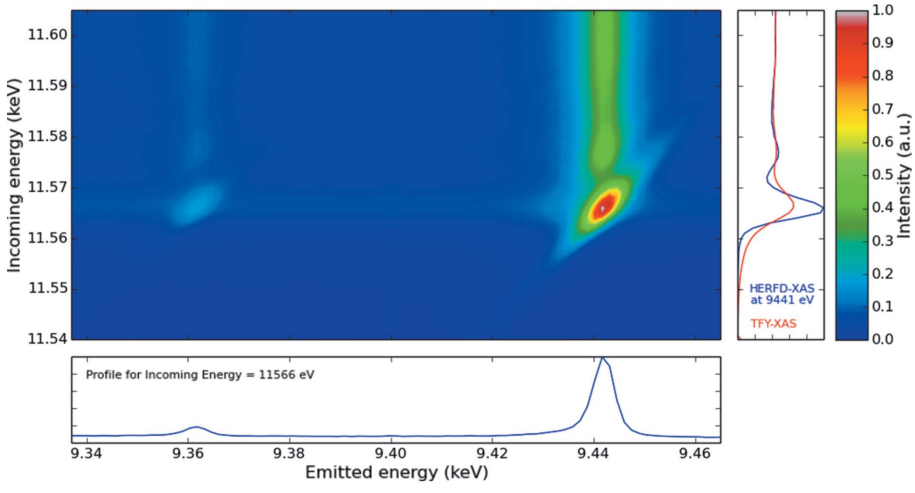

Figure 10
$L\alpha$ RXES map of hexachloroplatinic acid measured around the platinum L_3-edge using the von Hamos RXES installed at XDS. Total fluorescence yield (blue) and HERFD-XAS (red) data are shown on the right. The bottom pannel shows the resonant $L\alpha_1$ and $L\alpha_2$ XES spectra.

contribution, *i.e.* incident beam and spectrometer energy resolution.

The RXES data shown in Fig. 10 were measured in approximately 1 h; however, an excessively long acquisition time per incoming energy point was used in order to obtain data of excellent quality, in particular around the $L\alpha_2$ emission line (see above). Using a shorter integration time per point can decrease the total experimental time to less than 5 min.

3.4. Non-resonant X-ray emission spectroscopy

Non-resonant XES experiments are also interesting due to their capability of delivering information about the electronic structure, in particular about the details of the valence levels (Glatzel *et al.*, 2013; Gallo & Glatzel, 2014; Pollock & DeBeer, 2015). The $K\beta$ mainline of XES spectra is often used as an experimental fingerprint of the oxidation and spin states of the metal absorber (Gamblin & Urch, 2001; Glatzel & Bergmann, 2005), whereas the VtC region shows a unique sensitivity to the nature of the ligand bound to the metal (Pollock & DeBeer, 2011, 2015; Beckwith *et al.*, 2011; Gallo & Glatzel, 2014).

Density functional theory (DFT) is often used to model the VtC region in a straightforward one-electron scheme, as detailed in previous works (Lee *et al.*, 2010; Beckwith *et al.*, 2011; Pollock & DeBeer, 2011). Combination of experiment and DFT calculations has proved to be a powerful approach to obtain insight into the environment around a metal absorber, *e.g.* identification of a central carbide in the FeMo and FeV cofactors of nitrogenase (Lancaster *et al.*, 2011; Rees *et al.*, 2015), the discrimination of the two sub-complexes in [FeFe]-hydrogenase (Lambertz *et al.*, 2014). On the other hand, quantitative analysis of the $K\beta$ mainline region has been hindered by limitations associated with the computational approaches mostly used (Lee *et al.*, 2010; Lancaster *et al.*, 2011; Kumar *et al.*, 2013). Recently, Pollock *et al.* (2014) have improved the interpretation of the $K\beta$ mainlines by using restricted active space configuration interaction calculations (RAS-CI). This allowed the quantification of metal–ligand covalency and establishment of a relationship with the relative splitting observed in the $K\beta$ mainlines.

The capabilities of the von Hamos spectrometer installed at XDS to measure small signals was further demonstrated by measuring the $K\beta$ and VtC non-resonant XES spectrum of a Co_2O_3 solid sample (Fig. 11). To perform this experiment the incoming X-ray energy was set to 8.15 keV, which is above the Co *K*-edge absorption (7709 eV). A Ge(111) crystal analyzer was posed at a Bragg angle of about 82.9°. In this configuration the (444) reflection corresponds to an energy of approximately 7650 eV, which is close to the cobalt $K\beta$ emission lines. A total integration time of 3 h was used in order to obtain a good signal-to-noise ratio in the VtC region above 7670 eV. In this configuration the total energy resolution was 1.44 eV, with a contribution of 1.12 eV from the incoming beam. Thus, all the contributions to the final energy resolution in the von Hamos spectrometer amount to about 0.91 eV.

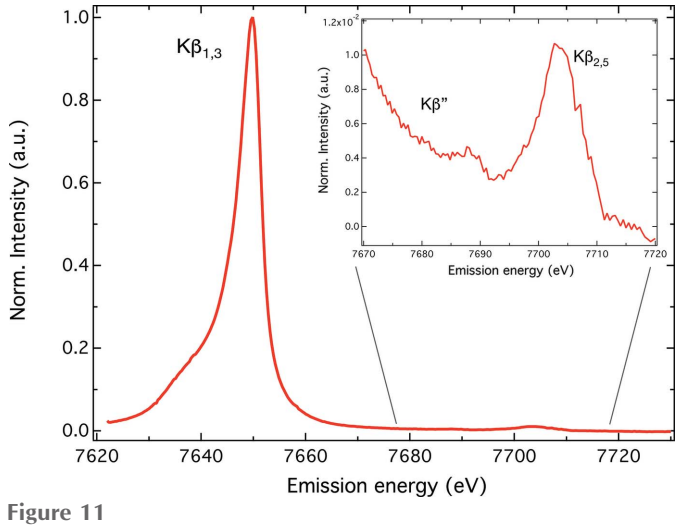

Figure 11
$K\beta_{1,3}$ and valence-to-core (VtC) X-ray emission spectrum for a Co_2O_3 sample recorded with the von Hamos spectrometer installed at XDS. During the data acquisition of this non-resonant XES spectrum neither beamline nor spectrometer components need to be scanned.

The XES spectrum in Fig. 11 contains the strong $K\beta_{1,3}$ emission line at 7650 eV and, at higher energy, the VtC emission at about 7705 eV. The inset in Fig. 11 shows that the VtC region consists of two main features, $K\beta''$ and $K\beta_{2,5}$. The $K\beta_{1,3}$ line arises from $3p \rightarrow 1s$ dipole-allowed transitions which are dominated by $3p$–$3d$ exchange correlation with a small contribution of $3p$ spin–orbit coupling, and the VtC features come from transitions from the filled ligand valence *ns* and *np* orbitals refilling the metal $1s$ core-hole (Pollock & DeBeer, 2011, 2015; Gallo & Glatzel, 2014). The quality of the obtained $K\beta$ XES spectrum allows a detailed analysis of line shape and position, as is commonly done with these data (Lee *et al.*, 2010; Pollock & DeBeer, 2011, 2015; Beckwith *et al.*, 2011; Pollock *et al.*, 2014; Boubnov *et al.*, 2014; Hugenbruch *et al.*, 2016; Kowalska *et al.*, 2016*a*). Furthermore, the relatively large energy range detected by von Hamos spectrometers allows the detection of several emission lines at once, which is useful in the case of multi-metal systems or when dealing with sensitive samples that do not stand the X-ray beam for long periods of time.

4. Discussion and conclusions

The multi-purpose materials science beamline XDS at the Brazilian synchrotron provides intense and high-energy (up to 30 keV) X-rays to the LNLS community. The three different crystal choices of the monochromator [plane Si(111), sagittal Si(111) and plane Si(311)] enable energies between 5 keV and 30 keV to be reached, with both focused or collimated beam, according to experimental needs. The beamline is suitable for regular XAS experiments in transmission or fluorescence modes, and XRD experiments can be performed using the heavy-duty 6+2-circle Huber diffractometer.

The XDS beamline is equipped with a broad range of detectors and equipment allowing experiments under non-ambient conditions: temperatures varying from <2 K up

to 1200 K, high magnetic fields up to 6 T, high pressures up to about 80 GPa, and also *in situ*/*in operando* conditions. Analysis of the polarization of the diffracted X-rays is also possible *via* the combination of the goniometers in the Huber diffractometer, polarimeter and crystal analyzers. Moreover, combined XAS–XRD experiments can be performed by exploiting the unique beam characteristics at LNLS. Novel experimental techniques at LNLS, *e.g.* X-ray total scattering, X-ray diffraction at high pressures, resonant/non-resonant X-ray emission spectroscopy with high energy resolution and XAS at high energies (above 18 keV) are becoming routine at XDS (Boita *et al.*, 2014; Saleta *et al.*, 2014; Saccone *et al.*, 2015; Hunt *et al.*, 2015).

5. Related literature

The following references are mentioned in the supporting information: Larson & Von Dreele (2000), NIST (2005), Rietveld (1969), Toby (2001).

Acknowledgements

The authors would like to thank all LNLS staff involved in the design, construction, commissioning and operation of XDS, in particular Régis T. Neuenschwander, Flávio Rodrigues, James F. Citadini, Joacir E. dos Santos, André L. Mesa, James R. Piton, Sergio R. Marques and Carlos R. Scorzato. We also acknowledge Dr Agustín Picco for kindly providing the silver nanoparticles. We are grateful for the financial support from FAPESP (project 2009/54115-8) and FINEP (project 01.05.0721.00-27/0144) that covered most of the construction and equipping of the beamline. FAL acknowledges support from CNPq.

References

Agnihotri, S., Mukherji, S. & Mukherji, S. (2014). *RSC Adv.* **4**, 3974–3983.
Alonso-Mori, R., Kern, J., Sokaras, D., Weng, T.-C., Nordlund, D., Tran, R., Montanez, P., Delor, J., Yachandra, V. K., Yano, J. & Bergmann, U. (2012). *Rev. Sci. Instrum.* **83**, 073114.
Alonso-Mori, R., Sokaras, D., Zhu, D., Kroll, T., Chollet, M., Feng, Y., Glownia, J. M., Kern, J., Lemke, H. T., Nordlund, D., Robert, A., Sikorski, M., Song, S., Weng, T.-C. & Bergmann, U. (2015). *J. Synchrotron Rad.* **22**, 612–620.
Ament, L. J. P., van Veenendaal, M., Devereaux, T. P., Hill, J. P. & van den Brink, J. (2011). *Rev. Mod. Phys.* **83**, 705–767.
Bastús, N. G., Merkoçi, F., Piella, J. & Puntes, V. (2014). *Chem. Mater.* **26**, 2836–2846.
Beckwith, M. A., Roemelt, M., Collomb, M.-N., DuBoc, C., Weng, T.-C., Bergmann, U., Glatzel, P., Neese, F. & DeBeer, S. (2011). *Inorg. Chem.* **50**, 8397–8409.
Bergamaschi, A., Cervellino, A., Dinapoli, R., Gozzo, F., Henrich, B., Johnson, I., Kraft, P., Mozzanica, A., Schmitt, B. & Shi, X. (2010). *J. Synchrotron Rad.* **17**, 653–668.
Bergmann, U., Glatzel, P., Robblee, J. H., Messinger, J., Fernandez, C., Cinco, R., Visser, H., McFarlane, K., Bellacchio, E., Pizarro, S., Sauer, K., Yachandra, V. K., Klein, M. P., Cox, B. L., Nealson, K. H. & Cramer, S. P. (2001). *J. Synchrotron Rad.* **8**, 199–203.
Bergmann, U., Horne, C. R., Collins, T. J., Workman, J. M. & Cramer, S. P. (1999). *Chem. Phys. Lett.* **302**, 119–124.
Billinge, S. J. L. (2004). *Z. Kristallogr.* **219**, 117–121.
Boita, J., Bernardi, F., Castegnaro, M. V., Nicolao, L., Alves, M. C. M. & Morais, J. (2014). *J. Phys. Chem. C*, **118**, 5538–5544.
Boubnov, A., Carvalho, H. W. P., Doronkin, D. E., Günter, T., Gallo, E., Atkins, A. J., Jacob, C. R. & Grunwaldt, J.-D. (2014). *J. Am. Chem. Soc.* **136**, 13006–13015.
Cezar, J. C., Fonseca, P. T., Rodrigues, G. L. M. P., de Castro, A. R. B., Neuenschwander, R. T., Rodrigues, F., Meyer, B. C., Ribeiro, L. F. S., Moreira, A. F. A. G., Piton, J. R., Raulik, M. A., Donadio, M. P., Seraphim, R. M., Barbosa, M. A., de Siervo, A., Landers, R. & de Brito, A. N. (2013). *J. Phys. Conf. Ser.* **425**, 072015.
Craievich, A. F. & Rodrigues, A. R. D. (1997). *Braz. J. Phys.* **27**, 417–424.
Döring, G., Sternemann, C., Kaprolat, A., Mattila, A., Hämäläinen, K. & Schülke, W. (2004). *Phys. Rev. B*, **70**, 085115.
Dykhne, T., Taylor, R., Florence, A. & Billinge, S. J. L. (2011). *Pharm. Res.* **28**, 1041–1048.
Egami, T. & Billinge, S. (2003). Editors. *Underneath the Bragg Peaks: Structural Analysis of Complex Materials*, 1st ed. New York: Pergamon.
Eisenberger, P., Platzman, P. M. & Winick, H. (1976). *Phys. Rev. Lett.* **36**, 623–626.
Farrow, C. L., Juhás, P., Liu, J. W., Bryndin, D., Bzin, E. S., Bloch, J., Proffen, Th. & Billinge, S. J. L. (2007). *J. Phys. Condens. Matter*, **19**, 335219.
Figueroa, S. J. A., Gibson, D., Mairs, T., Pasternak, S., Newton, M. A., Di Michiel, M., Andrieux, J., Christoforidis, K. C., Iglesias-Juez, A., Fernández-García, M. & Prestipino, C. (2013). *J. Appl. Cryst.* **46**, 1523–1527.
Gallo, E. & Glatzel, P. (2014). *Adv. Mater.* **26**, 7730–7746.
Gamblin, S. D. & Urch, D. S. (2001). *J. Electron Spectrosc. Relat. Phenom.* **113**, 179–192.
Glatzel, P. & Bergmann, U. (2005). *Coord. Chem. Rev.* **249**, 65–95.
Glatzel, P., Bergmann, U., Yano, J., Visser, H., Robblee, J. H., Gu, W., de Groot, F. M. F., Christou, G., Pecoraro, V. L., Cramer, S. P. & Yachandra, V. K. (2004). *J. Am. Chem. Soc.* **126**, 9946–9959.
Glatzel, P., Weng, T.-C., Kvashnina, K., Swarbrick, J., Sikora, M., Gallo, E., Smolentsev, N. & Mori, R. A. (2013). *J. Electron Spectrosc. Relat. Phenom.* **188**, 17–25.
Groot, F. de (2001). *Chem. Rev.* **101**, 1779–1808.
Groot, F. de & Kotani, A. (2008). *Core Level Spectroscopy of Solids.* Boca Raton: CRC Press.
Guimarães, B. G., Sanfelici, L., Neuenschwander, R. T., Rodrigues, F., Grizolli, W. C., Raulik, M. A., Piton, J. R., Meyer, B. C., Nascimento, A. S. & Polikarpov, I. (2009). *J. Synchrotron Rad.* **16**, 69–75.
Hall, E. R., Pollock, C. J., Bendix, J., Collins, T. J., Glatzel, P. & DeBeer, S. (2014). *J. Am. Chem. Soc.* **136**, 10076–10084.
Hämäläinen, K., Siddons, D. P., Hastings, J. B. & Berman, L. E. (1991). *Phys. Rev. Lett.* **67**, 2850–2853.
Hammersley, A. P., Svensson, S. O., Hanfland, M., Fitch, A. N. & Häusermann, D. (1996). *High. Press. Res.* **14**, 235–248.
Haverkamp, R. G. & Wallwork, K. S. (2009). *J. Synchrotron Rad.* **16**, 849–856.
Henglein, A. (1979). *J. Phys. Chem.* **83**, 2209–2216.
Hoszowska, J. & Dousse, J.-C. (2004). *J. Electron Spectrosc. Relat. Phenom.* **137–140**, 687–690.
Hugenbruch, S., Shafaat, H. S., Krämer, T., Delgado-Jaime, M. U., Weber, K., Neese, F., Lubitz, W. & DeBeer, S. (2016). *Phys. Chem. Chem. Phys.* **18**, 10688–10699.
Hunt, S. T., Kokumai, T. M., Zanchet, D. & Román-Leshkov, Y. (2015). *J. Phys. Chem. C*, **119**, 13691–13699.
Ingham, B. (2015). *Crystallogr. Rev.* **21**, 229–303.
Juhás, P., Davis, T., Farrow, C. L. & Billinge, S. J. L. (2013). *J. Appl. Cryst.* **46**, 560–566.
Kern, J., Hattne, J., Tran, R., Alonso-Mori, R., Laksmono, H., Gul, S., Sierra, R. G., Rehanek, J., Erko, A., Mitzner, R.,Wernet, P., Bergmann, U., Sauter, N. K., Yachandra, V. & Yano, J. (2014). *Philos. Trans. Roy. Soc. B*, **369**, 20130590.

Kotani, A. & Shin, S. (2001). *Rev. Mod. Phys.* **73**, 203–246.
Kowalska, J. K., Hahn, A. W., Albers, A., Schiewer, C. E., Bjornsson, R., Lima, F. A., Meyer, F. & DeBeer, S. (2016*a*). *Inorg. Chem.* **55**, 4485–4497.
Kowalska, J. K., Lima, F. A., Pollock, C. J., Rees, J. A. & DeBeer, S. (2016*b*). *Israel J. Chem.*, http://dx.doi.org/10.1002/ijch.201600037.
Krause, M. O. & Oliver, J. H. (1979). *J. Phys. Chem. Ref. Data*, **8**, 329–338.
Kumar, P., Nagarajan, R. & Sarangi, R. (2013). *J. Mater. Chem. C*, **1**, 2448–2454.
Lambertz, C., Chernev, P., Klingan, K., Leidel, N., Sigfridsson, K. G. V., Happe, T. & Haumann, M. (2014). *Chem. Sci.* **5**, 1187–1203.
Lancaster, K. M., Finkelstein, K. D. & DeBeer, S. (2011). *Inorg. Chem.* **50**, 6767–6774.
Larson, A. C. & Von Dreele, R. B. (2000). *General Structure Analysis System (GSAS)*. Los Alamos National Laboratory, New Mexico, USA.
Lee, N., Petrenko, T., Bergmann, U., Neese, F. & DeBeer, S. (2010). *J. Am. Chem. Soc.* **132**, 9715–9727.
Lee, P. C. & Meisel, D. (1982). *J. Phys. Chem.* **86**, 3391–3395.
Lima, J. C. de, Ferreira, A. & de Biasi, R. (2016). *J. Non-Cryst. Solids*, **447**, 21–28.
Lima, J. C. de, Poffo, C., Souza, S., Machado, K., Trichês, D. M., Grandi, T. & de Biasi, R. (2013). *Phys. B*, **424**, 60–68.
Loula, G., dos Reis, R., Haskel, D., Garcia, F., Souza-Neto, N. & Gandra, F. (2012). *Phys. Rev. B*, **85**, 245128.
Mattern, B. A., Seidler, G. T., Haave, M., Pacold, J. I., Gordon, R. A., Planillo, J., Quintana, J. & Rusthoven, B. (2012). *Rev. Sci. Instrum.* **83**, 023901.
Meisel, A., Leonhardt, G. & Szargan, R. (1989). *X-ray Spectra and Chemical Binding.* Berlin: Springer.
Moreno, G., Bongers, R., Cardoso, M., O'Dowd, F. & Slepicka, H. (2015). *Proceedings of the 15th International Conference on Accelerator and Large Experimental Physics Control Systems (ICALEPCS2015)*, pp. 1119–1122. Melbourne, Australia.
Moreno, T., Westfahl, H., Freitas, R. de O., Petroff, Y. & Dumas, P. (2013). *J. Phys. Conf. Ser.* **425**, 142003.
Nemoshkalenko, V. V., Mindlina, M. A. & Mamko, B. P. (1968). *Phys. Status Solidi B*, **30**, 703–712.
NIST (2005). Certicate of Analysis, Standard Reference Material 676. Gaithersburg, Maryland, USA.
Petkov, V. (2012). *Charact. Mater. Chap. Pair Distrib. Functions Anal.* pp. 1361–1372 Willey.
Petkov, V., Ren, Y., Kabekkodu, S. & Murphy, D. (2013). *Phys. Chem. Chem. Phys.* **15**, 8544–8554.
Pollock, C. J. & DeBeer, S. (2011). *J. Am. Chem. Soc.* **133**, 5594–5601.
Pollock, C. J. & DeBeer, S. (2015). *Acc. Chem. Res.* **48**, 2967–2975.
Pollock, C. J., Delgado-Jaime, M. U., Atanasov, M., Neese, F. & DeBeer, S. (2014). *J. Am. Chem. Soc.* **136**, 9453–9463.
Rees, J. A., Bjornsson, R., Schlesier, J., Sippel, D., Einsle, O. & DeBeer, S. (2015). *Angew. Chem. Int. Ed.* **54**, 13249–13252.
Rietveld, H. M. (1969). *J. Appl. Cryst.* **2**, 65–71.
Rivas, L., Sánchez-Cortes, S., García-Ramos, J. V. & Morcillo, G. (2001). *Langmuir*, **17**, 574–577.
Rodella, C. (2015). Private communication.
Rodrigues, A. R. D., Craievich, A. F. & Gonçalves da Silva, C. E. T. (1998). *J. Synchrotron Rad.* **5**, 1157–1161.
Rueff, J.-P. & Shukla, A. (2013). *J. Electron Spectrosc. Relat. Phenom.* **188**, 10–16.
Saccone, F. D., Ferrari, S., Errandonea, D., Grinblat, F., Bilovol, V. & Agouram, S. (2015). *J. Appl. Phys.* **118**, 075903.
Safonov, V. A., Vykhodtseva, L. N., Polukarov, Y. M., Safonova, O. V., Smolentsev, G., Sikora, M., Eeckhout, S. G. & Glatzel, P. (2006). *J. Phys. Chem. B*, **110**, 23192–23196.
Safonova, O. V., Tromp, M., van Bokhoven, J. A., de Groot, F. M. F., Evans, J. & Glatzel, P. (2006). *J. Phys. Chem. B*, **110**, 16162–16164.
Saleta, M., Mastelaro, V. & Granado, E. (2014). *Acta Cryst.* A**70**, C872.
Sanchez del Rio, M., Canestrari, N., Jiang, F. & Cerrina, F. (2011). *J. Synchrotron Rad.* **18**, 708–716.
Schmitt, B., Brönnimann, C., Eikenberry, E. F., Hülsen, G., Toyokawa, H., Horisberger, R., Gozzo, F., Patterson, B., Schulze-Briese, C. & Tomizaki, T. (2004). *Nucl. Instrum. Methods Phys. Res. A*, **518**, 436–439.
Schmitt, B., Brönnimann, C., Eikenberry, E. F., Gozzo, F., Hörmann, C., Horisberger, R. & Patterson, B. (2003). *Nucl. Instrum. Methods Phys. Res. A*, **501**, 267–272.
Souza-Neto, N. M., Zhao, J., Alp, E. E., Shen, G., Sinogeikin, S. V., Lapertot, G. & Haskel, D. (2012). *Phys. Rev. Lett.* **109**, 026403.
Swanson, H. E. & Tatge, E. (1953). US National Bureau of Standards Circular 539, pp. 1–95.
Syassen, K. (2008). *High. Press. Res.* **28**, 75–126.
Szlachetko, J., Nachtegaal, M., de Boni, E., Willimann, M., Safonova, O., Sa, J., Smolentsev, G., Szlachetko, M., van Bokhoven, J. A., Dousse, J.-C., Hoszowska, J., Kayser, Y., Jagodzinski, P., Bergamaschi, A., Schmitt, B., David, C. & Lcke, A. (2012). *Rev. Sci. Instrum.* **83**, 103105.
Tanaka, S., Okada, K. & Kotani, A. (1994). *J. Phys. Soc. Jpn*, **63**, 2780–2787.
Toby, B. H. (2001). *J. Appl. Cryst.* **34**, 210–213.